A rotating holographic imager for stationary cloud droplet and ice crystal measurements

Ville A. Kaikkonen[1] · **Eero O. Molkoselkä[2]** · **Anssi J. Mäkynen[2]**

Abstract

An optical cloud droplet and ice crystal measurement system ICEMET (icing condition evaluation method), designed for present icing condition monitoring in field conditions, is presented. The aim in this work has been to develop a simple but precise imaging technique to measure the two often missing parameters needed in icing rate calculations caused by icing clouds—the droplet size distribution (DSD) and the liquid water content (LWC) of the air. The measurement principle of the sensor is based on lens-less digital in-line holographic imaging. Cloud droplets and ice crystals are illuminated by a short laser light pulse and the resulting hologram is digitally sampled by a digital image sensor and the digital hologram is then numerically analyzed to calculate the present DSD and LWC values. The sensor has anti-icing heating power up to 500 W and it is freely rotating by the wind for an optimal sampling direction and aerodynamics. A volume of 0.5 cm^3 is sampled in each hologram and the maximum sampling rate is 3 cm^3/s. Laboratory tests and simulations were made to ensure the adequate operation of the measurement sensor. Computational flow dynamics simulations showed good agreement with droplet concentration distributions measured from an icing wind tunnel. The anti-icing heating of the sensor kept the sensor operational even in severe icing conditions; the most severe test conditions were the temperature -15 °C, wind speed 20 m/s and the LWC 0.185 g/m^3. The verification measurements made using NIST traceable monodisperse particle standard glass spheres showed that the ICEMET sensor measurement median diameter 25.54 μm matched well with 25.60 μm $\pm$ 0.70 μm diameter confidence level given by the manufacturer.

Keywords Laser · Imaging systems · Meteorology · Optical instruments · Digital holography · Icing

1 Introduction

Monitoring of icing conditions in cold regions has gained more interest in recent years, mainly due to the rapid increase in wind power [1]. To model atmospheric icing adequately it is needed to know not just the parameters routinely measured in many sites such as the temperature, the humidity and the wind speed, but also the present LWC and the DSD [2]. At present, there is no standardized way of measuring these parameters for the low-level clouds [3]. Many different types of academic research and commercial instruments have been developed to measure these properties from cloud droplets, and they have been realized both as airborne and stationary instruments [4–9]. Up to date, these instruments have been used mostly for academic research purposes, but none of the LWC and DSD measuring instruments have found their way for a large-scale operational use for example in wind energy production in cold climates, despite the need for such instruments has been noted at early stage [1, 10].

To address the issue of inadequate measurement data of DSD and LWC from icing field conditions, we present a novel optical instrument with a very simple and rigid optical construction, based on the digital holographic imaging of the droplets and ice crystals. In recent years, the time required to reconstruct digital holograms has decreased rapidly by the use of graphics processing units (GPU),

✉ Ville A. Kaikkonen
  ville.kaikkonen@oulu.fi

1 Unit of Measurement Technology, University of Oulu, Technology Park P.O. Box 127, 87400 Kajaani, Finland

2 Optoelectronics and Measurement Techniques Unit, University of Oulu, P.O. Box 4500, 90014 Oulu, Finland

enabling the use of digital holography in many nearly real-time applications. Today, the digital holographic imaging techniques have found their usage for example in many medical and biological applications, in security applications, as well as in particle velocimetry [11–17].

In-line holography in its simplest form, also named after its founder as Gabor geometry, is suited for imaging small objects through a medium which is mainly transparent [18, 19]. Instruments for cloud droplet measurement based on the holographic in-line imaging of cloud droplets have been reported both on film and on digital image sensors [4, 9, 20–22]. To our best knowledge, this is the first digital cloud sampling holographic instrument designed for long-term use in arctic environmental conditions and utilizing a structure to sample the clouds consistently independent of the wind direction. The measurement principle of the instrument presented is lens-less digital holographic imaging using point light source. In this paper, we present the fundamental design behind the ICEMET sensor and show results from NIST traceable sizing verification, simulations and measurement test results on the sampling of the instrument, field measurement installation and results and processing times of the recorded holograms.

2 Materials and methods

The holographic imaging principle using a point light is discussed in the context of cloud droplet imaging and measurement. Practical design considerations that were made to develop the ICEMET sensor for cloud droplet and ice crystal measurement are presented.

2.1 Holographic imaging

Digital holographic imaging is a technique where a complex diffraction pattern, a hologram, is first recorded on a digital image sensor and later processed digitally. A hologram is formed when the coherent light from the light source scatters from the objects and interferes with the other parts of the light field from the light source and is then captured as measurable intensity variations by the digital image sensor pixels. The size and the location of each object between the light source and digital image sensor are encoded in the hologram as diffraction pattern, and they can be obtained when the hologram is reconstructed numerically by back-propagating the light field. From the reconstructed light field, the grayscale shadow images of the objects can be formed by numerically focusing at different depths from the hologram [23, 24].

2.2 Design requirements for the cloud droplet and ice crystal holographic imager

The cloud droplets are considered water droplets with up to 200 μm diameters, although there is no strict definition of the size range [25]. The larger the droplet is, the less the droplet alters its trajectory with the airflow when the clouds encounter obstacles [2]. The droplets with larger diameters carry significantly larger amount of water compared with the smaller droplets (the power of three dependency of volume vs. diameter). A single parameter used in icing models to describe the DSD is the median volume diameter (MVD). The MVD value is a calculated, non-real, droplet size, which is calculated as the droplet size that divides the total water content sum of the DSD in half. Meaning that half of the total water content of the DSD is in the droplets with a smaller diameter than the MVD and similarly the other half of the total water content in droplets with a larger diameter than the MVD [26, 27]. It is important to be able to measure the DSD, and not solely the LWC, as the same LWC with higher MVD has the same water content with a larger proportion of the large droplets, which are more likely to collide with structure and cause ice accretion. The main size range of interest for icing rate measurement is in the 10–30 μm range [6, 28, 29]. In the ICEMET sensor design, we aimed to be able to measure the droplets and ice crystals larger than approx. 5 μm in diameter, so that the most significant size range would not be at the edge of the resolving power limit.

The measurement volume should always be orthogonal in respect in the direction of the wind to minimize the effects that alter the flow of air through the sampling volume—turning the sensor by the wind guarantees that the wind direction should have a minimal effect on the sampling. As any instrument measuring cloud droplets and ice crystals in-situ always has some finite dimensions, the effect of the sensor housing on the sampling efficacy of the instrument should be considered [9, 30]. In the in-line holographic imaging geometry, the measurement volume is always located between the light source and the image sensor so that the measurement volume is limited between two protective windows in all practical field instrument configurations. The measurement volume length between the two protective windows should preferably be as large as possible for an undisturbed air flow, but the size of the image sensor, the expected droplet concentrations, the divergence and the wavelength of the laser diode limit the practical measurement volume dimensions than can be realized.

Holographic instruments for cloud droplet imaging have been typically based on in-line holographic imaging, but

the illumination has been made using a collimated laser beam [4, 9, 31]. The use of a collimated beam for hologram illumination leads to a unity magnification of the diffraction patterns in the hologram and thus expensive magnifying camera optics is needed for high resolving power systems. A simple and cost effective way to magnify the diffraction patterns on the hologram is to use point-like light source, where the nearly spherical waves from the point source create a varying magnification on the diffraction patterns on the hologram [23].

2.3 Imaging geometry of a digital lens-less in-line holographic imager utilizing a point light source

The basic components needed to construct a lens-less digital holographic microscopic imager are a laser diode with large enough divergence and a digital image sensor. The imaging volume formed by the point source and a square-shaped image sensor is a pyramid shape, Fig. 1.

2.4 The point light source

A conventional laser diode with large enough divergence can be used as a point light source without additional optics. A laser diode with single-mode operation and a relatively high optical pulsed power is needed for recording the magnified holograms of fast moving objects such as the cloud droplets. The laser is required to illuminate the hologram with high enough intensity, and the pulse length of the laser should be in the range of tens of nanoseconds for practical operation
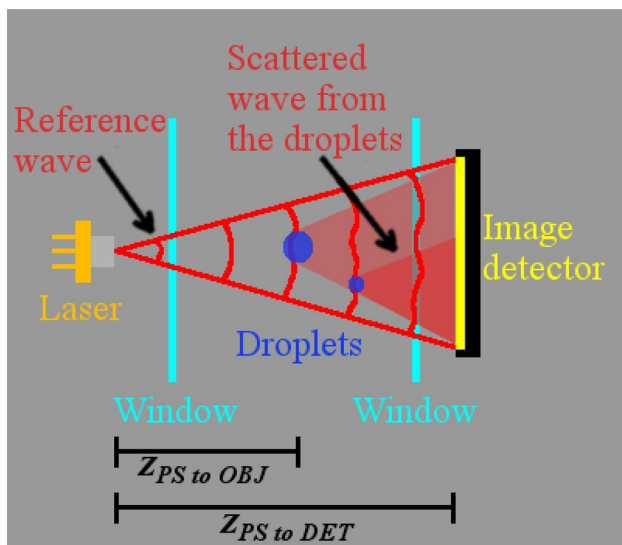
Fig. 1 An illustration of basic components needed to make a digital lens-less holographic imaging system with two protective windows for outdoor use

in high wind speeds to freeze the movement of the droplets and ice crystals in the holograms. The laser selected for this purpose was a 5.6 mm laser diode by Ushio Opto Semiconductors Inc., operating at 660 nm wavelength and rated maximum optical pulse power of approx. 300 mW. For the laser driver, a remote controlled driver unit was required, so that the laser driver parameters could be adjusted during the operation if needed. Multiple pulsing capability was a selection criterion for the pulse generator, as it makes possible to measure droplet velocities. The selected laser controller and laser driver come from PicoLAS GmpH; the USB-controlled pulse generator PLCS-21 and pulse laser diode driver LDP-V 03-100 V3.3 with adjustable pulse lengths from 1 ns up to 10 µs. The units are such large that they were not practical to install together with the laser inside the laser diode housing, as it would make the housing so large it would affect the air flow significantly. As a solution, a stripline for the laser diode was made from copper tape and Kapton® tape, so that the laser driver could be placed apart from the laser diode. The pulse length used is typically 50 ns, which is enough to freeze the moment of the objects to less than one pixel size in the hologram up to 30 m/s speed. The laser diode is driven approx. 1.5 times over the manufacturer specified maximum drive current of 350 mA. As the duty cycle in our application is very low in comparison with the given specifications, the laser diode is estimated to cool down enough between the pulses so that laser diode operating lifetime should not be affected greatly. The resulting higher optical power from the use of over current makes it possible to use lower gain in the image sensor, and thus increasing the signal-to-noise ratio on the holograms. The laser beam quality could be made better by spatially filtering the beam using a small pinhole, but this would need precise alignment, and such a design would be prone to any misalignment caused by vibrations [23]. As the instrument is designed for harsh environmental conditions were vibrations are very likely to happen often from different sources, the realization of the laser illumination was done without spatial filtering.

2.5 The image sensor

The image sensor's pixel size and density determine how small details and how large area of the hologram can be sampled. On the other hand, the image sensor area directly affects how large volumes can be sampled in to a single hologram in lens-less geometry. A suitable balance between resolving power, sampling volume and price and physical size of the sensor circuit board size was found with the 2/3″ image sensor size. To minimize the effect of the ambient light in the hologram, a sensor with short global shutter speed was preferred. The selected camera module with a greyscale Sony IMX264 image sensor has a minimum shutter time of 13 µs, and has a sensor with 2448 × 2048

of 3.45 μm size pixels, USB3 connection and maximum frame rate of 35 frames per second (fps). A 1″ diameter 40 nm band-pass filter at the central wavelength of 650 nm is placed directly in front of the image sensor to further reduce the amount of ambient light reaching the image sensor. Although the image sensor with USB3 is capable of delivering 35 fps, the slipring in the ICEMET sensor is capable only to provide USB2.0 connection, which reduces the data transfer rate significantly, and practical maximum frame rate has been found to be 6 fps using a USB2.0 connection.

2.6 Sensor mechanical and electrical design

The ICEMET sensor frame was built from machined aluminum parts, which were anodized with UV-resistant coating for outdoor use, joints between different parts are sealed with rubber gaskets. The amount of anti-icing heating power needed for the ICEMET sensor was adapted and estimated from the guidelines made for aircraft de-icing power dimensioning [32]. The power and data connection to the sensor through the rotating part is done using a slipring, with USB2.0 connection, power line with max. 20-A capacity and the lowest operation temperature of − 40 °C. The sensor is powered using operator safe 48 VDC voltage, which was selected to reach the estimated heating capacity of 500 W. The anti-icing functionality is realized by resistive heater elements glued inside the frame, and controlled by a programmable thermal controller with an external temperature sensor. The heating elements are placed so that most of the heating power is available near the measurement volume. All heating elements have an overheat protection thermostat which opens when the temperature rises above 45 °C.

In the ICEMET sensor, the sensor sampling volume is defined between as a 3 cm gap between two 10 cm disks. The disks are made as knife-edge designs to have better aerodynamical properties to minimize the unequal sampling of different sized droplets at different wind speeds. The measurement heads are tilted forward outwards in the wind direction to reduce the effect of the lower frame on the airflow near the measurement volume. The ICEMET sensor main parts are shown in Fig. 2. The height of the ICEMET sensor is 53 cm without a support arm and the weight is 8 kg. The knife-edge disks have a diameter of 10 cm and the air gap between the disks is 3 cm. The measurement volume and the optical axis are located between the centers of the opposite side disks.

2.7 The resolving power

The magnification M of the diffraction pattern on a hologram generated by a point light source at different distances z from the laser can be calculated as
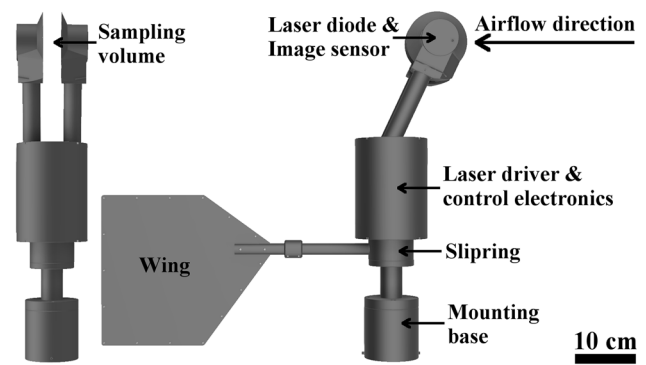

Fig. 2 The main parts of the ICEMET sensor. Front view on the left side, and side view on the right side

$$M(z) = {Z_{\text{PS to DET}}}\big/{Z_{\text{PS to OBJ}}}, \tag{1}$$

where $Z_{\text{PS to DET}}$ is the distance from the point source (laser diode) to the image sensor, and the $Z_{\text{PS to OBJ}}$ is the distance from the point source to the object. The resolving power of a holographic imaging device is limited by the wavelength and the numerical aperture (NA) as in all conventional optical imaging devices [23]. The achievable resolving power of a lens-less in-line holographic imaging setup is dependent on the wavelength of the light source, the distance between the light source and the image sensor and the size of the digital image sensor and its pixel size, as described in the following.

The size of the image sensor and the reconstruction distance ultimately define the numerical aperture in a lens-less in-line holographic imaging system. The effective sensor aperture D can be calculated as

$$D = \sqrt{w \times h}, \tag{2}$$

where w is the width of the sensor and h is the height of the sensor. The achievable NA at different distances z from the image sensor plane can be calculated as

$$\text{NA}(z) = \frac{D}{2 \times z}, \tag{3}$$

where D is the effective sensor aperture and z is the distance from the sensor plane. The smallest detectable circular disk diameter δ that the system can detect at different distances z from the image sensor, can be estimated using the Rayleigh criterion, just as in conventional imaging systems. The resolving power can be estimated to be

$$\delta(z) = 1.22 \frac{\lambda}{\text{NA}(z)}, \tag{4}$$

where λ is the wavelength of the laser and $\text{NA}(z)$ is the numerical aperture of the point source at distance z [23]. In practice, other factors also limit the achievable resolution, and largest of those is the pixel size of the image sensor,

which limits the smallest detectable diffraction fringe patterns that can be detected. To be able to resolve an object recorded in the reconstruction reliably, at least two image sensor pixels are needed [9, 31]. For a system using collimated illumination the magnification through the measurement volume is unity, only affected by the magnification of the imaging optics. When using a point light source, the magnification is different at all positions between the light source and the image sensor. The effective pixel size of the image sensor, Pix_{eff}, in a point source illumination system can be calculated by dividing the image sensor pixel size by the corresponding geometrical magnification. In this manner, the two-pixel effective pixel size limit, $\text{Pix}_{\text{eff}}(z)$, on the resolving power in the middle of the image at different distances z can be written as

$$\text{Pix}_{\text{eff}}(z) = 2 \times \frac{\text{px}}{M(z)}, \tag{5}$$

where px is the pixel size of the image sensor and the $M(z)$ is the geometrical magnification of the diffraction pattern at different reconstruction distances z. From these equations, the achievable resolving power in the middle of the imaging volume can be formed by plotting a graph where both this resolving power limiting factors are considered. On the image sensor side, the NA is very large, but $\text{Pix}_{\text{eff}}(z)$ value larger because of the lower magnification closer to the image sensor. On the laser diode side, the geometrical magnification is enlarging the diffraction pattern and the fringe spacing below the original pixel size, but then the image sensor size limits the achievable NA. When all limiting factors are plotted in to a graph together with the reconstruction distance z, the highest value of any limiting factor sets the maximum optical resolving power at that reconstruction distance. The maximum theoretical optical resolving power along the z-axis through the center of the whole imaging volume calculated using the component values in the ICEMET sensor are shown in Fig. 3.

3 Hologram reconstruction and data processing

The holograms captured with the ICEMET sensor are reconstructed and analyzed using a custom made multi-threaded and GPU accelerated software ICEMET-Server [33]. ICEMET-Server is compatible with any GPU that supports OpenCL™ (Open Computing Language) version 1.2 [34]. For better performance, a GPU with at least 8 GB of video memory is recommended. The software is in most parts based on methods described in [35].

The digital hologram recorded with the image detector is a grayscale intensity image, which has been formed from
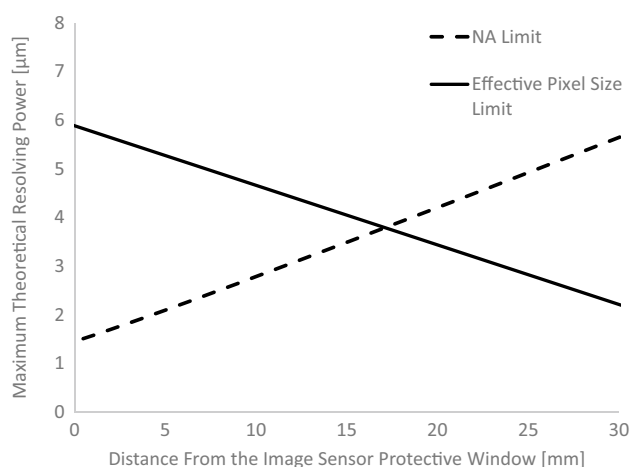
Fig. 3 The maximum optical resolving power at different reconstruction distances between the two protective windows on the ICEMET sensor. Image sensor side protective window at distance of 0 mm, and laser diode protective window at position 30 mm. According to these criterions, the resolving power varies between 3.8 and 6 μm through the whole volume

the interference of two electrical fields; the reference wave E_{Ref} originating from the laser and the light scattered by the objects located between the laser and the image detector E_{Obj}. The total electrical field E_{Tot} at the image detector can be written as

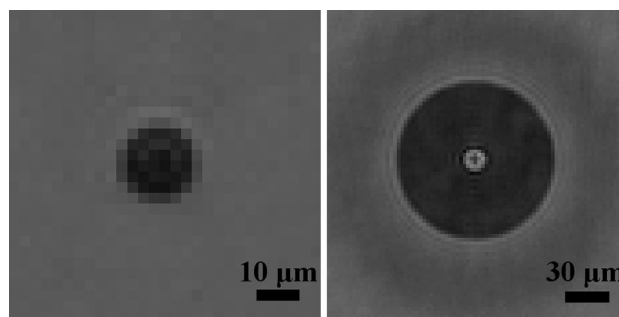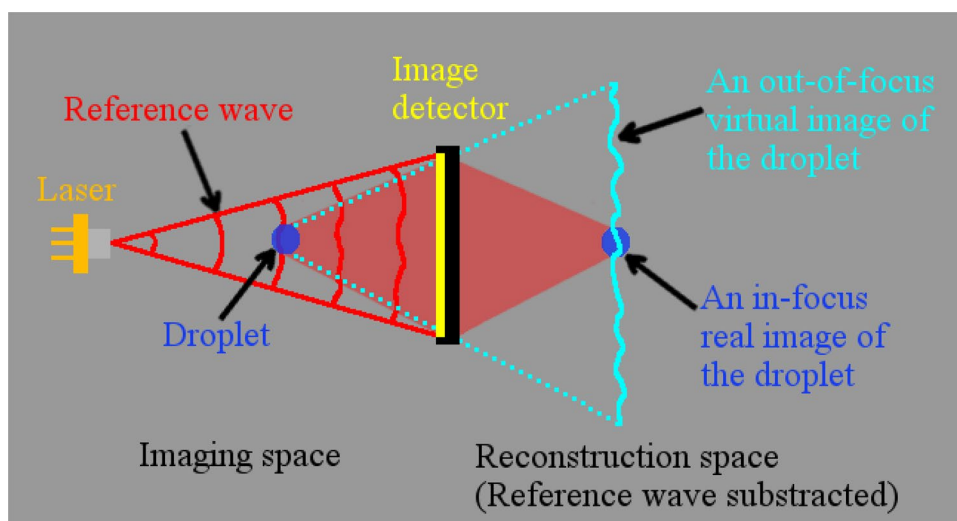$$E_{\text{Tot}}(x, y) = E_{\text{Ref}} + E_{\text{Obj}}. \tag{6}$$

The image detector is not able to sample just any electrical field, but rather the superposed waves over multiple periods, which form a two-dimensional intensity pattern I_{Det} on the image detector. This recorded intensity pattern can be written as

$$I_{\text{Det}}(x, y) = E_{\text{Tot}} E_{\text{Tot}}^* = E_{\text{Ref}} E_{\text{Ref}}^* + E_{\text{Ref}} E_{\text{Obj}}^* + E_{\text{Obj}} E_{\text{Ref}}^* + E_{\text{Obj}} E_{\text{Obj}}^*, \tag{7}$$

where all the last four terms are present in the hologram as discussed in the following. The first term is the dc term, the constant background, of the sole reference wave, which does not contain any information about the objects in the hologram and should be removed before reconstructing the hologram [36]. In our system, the dc term is removed by subtracting a background hologram from each recorded hologram, which yields in a so-called contrast hologram. The background hologram is generated from pixel-by-pixel median of seven neighboring sequential holograms. The method eliminates stationary fringes resulting from reflections or dust or droplets stuck on the windows but retains all the moving particles. The second term in Eq. 7 contains the information about the actual object of interest and is called the real image. The third term is called the virtual image, or

the twin image; it is essentially the same image of the object of interest as in the second term, but the virtual image is located at the opposite direction with respect to the image sensor in the reconstruction. In the in-line geometry, the virtual image overlaps with the real image in the axial direction. It is an unwanted term, which is inherent in this simple in-line hologram recording geometry. However, two aspects of the imaging system and its application minimize the virtual image term to be negligible in practical use. First, the point source geometry makes the virtual images appear magnified at the in-focus position of the real image [37]. The magnified virtual image is, therefore, seen as a largely blurred image of the object in the background on the focal plane of the real image, Fig. 4. The virtual images of droplets thus increase the noise level in the reconstructions. If there would be tens of thousands to millions of particles in a single hologram, they would severely degrade the hologram [38]. But for the density of cloud droplets in natural environment, the amount of droplets is typically from hundreds to thousands droplets per frame and thus does not increase the noise level significantly. Second, as the objects of interested, the cloud droplets and crystals, are fairly small in size, typically just 5–30 μm in diameter, the axial extent when they are blurred is short, and therefore, the virtual image over the real image is blurred to undetectable background noise [35]. The effect of the virtual image can be seen in the hologram reconstructions of the largest droplets, which are located close to the image sensor, and hence the virtual image is closer to the reconstructed plane. This can be seen as a darker ring-shaped pattern around the droplets as in Fig. 5, which needs to be noted when selecting a suitable threshold for binarizing the image. To avoid selecting a false background level because of the effect of virtual images on the reconstructed image planes, we calculate the binarization threshold value from the whole hologram area as a global value. The fourth

Fig. 5 Two reconstructed droplet images at a distance of 6.4 mm from the camera side window. The left droplet was analyzed to have an equivalent diameter of 18 μm and the droplet on the right side similarly 109 μm. The effect of the virtual image can be seen as a darker ring around the larger droplet, but it is negligible on the image of the smaller droplet

term in the Eq. 7 is the mutual interference of the scattered waves from the objects, which is a negligible part in the hologram in the case of cloud droplets as the amplitude of the scattered waves from the small diameter droplets are much smaller than the amplitude of the reference wave. Therefore, when reconstructing the contrast hologram the real image term dominates in the focal plane of objects, which enables in-focus reconstructions of the shadow images of the droplets and ice crystals with relatively low background noise caused by the virtual images.

ICEMET-Server reads the recorded hologram image files from a path and pre-processes them. The preprocessing phase consists of cropping and dividing each hologram by a background image. Hologram images are cropped to square-shapes of 2048×2048 pixels, which results in more evenly illuminated holograms. The smaller number of pixels in the holograms after cropping decreases also the processing time. Hologram reconstruction is performed by propagating the

Fig. 4 The overlapping of the in-focus real image and the out-of-focus virtual image of the cloud droplet at the reconstruction plane in the in-line holographic recording geometry using a point source

wave field using the angular spectrum method. Filtering kernel H is applied to the image in frequency domain

$$H(u, v, z) = \exp\left(-jkz\sqrt{1 - (\lambda u)^2 - (\lambda v)^2}\right), \tag{8}$$

where u and v represent the distances from the center of the image sensor and z the reconstruction distance in z-axis.

The whole measurement depth is reconstructed into an image stack and an intensity minimum image of the whole reconstruction range is generated simultaneously. From the minimum image the x- and y-coordinates of the particles can be extracted. With these co-ordinates, the particle segments are extracted from the minimum image. Next, the best focus distances of the particles in these segments are searched along the z-axis using two different scoring methods: the minimum intensity for the smaller segments (width and height < 5 pixels) and the maximum variance of a standard deviation filtered segment for the larger segments.

It has been shown that the focus algorithms based on minimum intensity value can result in a small focus plane offset in comparison with the real position of the objects [39, 40]. However, in this application, the main interested is not to measure precisely the particle 3D positions, but to target precise real-time measurement of the particle sizes and numbers to determine the LWC and the MVD values. When using a point source illumination, the accuracy of the focus position has an effect on the value of the effective pixel size in the found focus plane. Thus, the accuracy of the particle size measurement depends on the focusing accuracy. However, in our case, it has a negligible effect as the effective pixel size is almost constant within the focus uncertainty range, the focus offset would need to be several millimeters to cause major uncertainty to the particle measurement results. Thus in this application, the offset caused by focus based on intensity values can be neglected as it has a minimal effect on the size estimation of the droplets and ice crystals. The benefit of using intensity based focus merits is that they are not computationally expensive functions, which is essential in real-time applications.

The highest focus score is estimated using a greedy algorithm based on ternary search. The execution time is ten times lower in comparison with iterating through the whole reconstruction stack while not missing any of the particles. This is possible because our scoring functions produce high global peaks.

ICEMET-Server supports both a reconstruction in slices and the reconstruction of the whole measurement depth at once. Generally using less slices is faster and more reliable but requires more GPU memory. For a reference, reconstructing the whole range of ICEMET sensor in one slice with 20 μm step requires storing over 1500 reconstructed images which translate to 5.9 GiB of data. This is why slicing the reconstruction range is necessary when using limited hardware resources.

The found best-focus grayscale intensity images are binarized to calculate the particle properties. Image binarization threshold value I_{th} for reconstructed particles is obtained as

$$I_{th} = I_{bg} - f_{th}(I_{bg} - I_{min}), \tag{9}$$

where I_{min} is the local minimum, f_{th} is a threshold factor $(= 0.35)$ and I_{bg} is the global background intensity which is estimated as the median of the image. Size and shape features are extracted from binarized particle images using standard image processing functions. The DSD values are calculated from the droplet equivalent diameters. The LWC is calculated as spherical fits from the droplet equivalent diameters and the known measurement volume. The MVD values are calculated from the DSD histograms as described in [41]. The calculated shape features can be used to distinguish droplets from other objects such as ice crystals, insects or pollen, for example.

The obtained particle and statistical data are written into an SQL database and focused and binarized particle images are saved in the filesystem. ICEMET-Server also generates preview images that show all of the particles flattened to one surface. The database can be accessed with any compatible SQL client or ICEMET web interface software, Fig. 6.
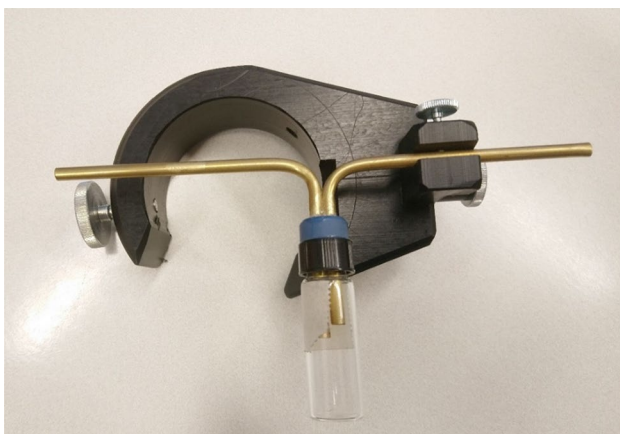
4 Results

4.1 Sizing verification using NIST traceable glass spheres

The ICEMET sensor sizing was verified using NIST traceable monodisperse particle standard glass beads from Whitehouse Scientific Ltd. The beads used for calibration have a median size of 25.60 μm with an uncertainty of ± 0.70 μm. The beads were mixed in the air using an in-house made dispenser, Fig. 7. The dispenser was first used with compressed clean air can, but it was noted that because the air from the bottle is not the same as the room temperature, the air stream in holograms was visible and thus affecting the background of the holograms. For this reason, we changed the air can to a manual air blow pump (Tornado Blower), where the air blown is taken by a valve from the ambient air. The downside of this type of blower is that there is a possibility of blowing dust from the room air with the beads to the calibration, but only a few dust particles were noted, and they could be removed from the calibration results based on their shape, as well as any particles that were attached to gather in clusters. The result after calibration using results from 11,995 measured beads shown in Fig. 8, the median size (D50) measured by the ICEMET sensor was 25.54 μm,

Fig. 6 ICEMET web interface. Actual reconstructed grayscale particle images in the Particle-column, in the Threshold-column are the binarized image of the particle. In the Preview-column all the particles found in the hologram analysis are shown in a single image. Other columns present the most used parameters for statistical analyses; most importantly in the EquivDiameter-column is the area equivalent circle diameter for each object

| Home | Images ▾ | Histograms ▾ | Statistics ▾ | Database | Help |

```
ID, DateTime, Sensor, Frame, Particle, X, Y, Z, EquivDiam, EquivDiamCorr, Circularity,
DynRange, EffPxSz, SubX, SubY, SubW, SubH
```

≤ 1 ≥

ID	DateTime	Particle	Threshold	Preview	EquivDiam (µm)	Z (mm)	HeywoodCircFact	DynamicRange
224966	2017-02-12 16:18:30				89	16.280	1.33	120
225278	2017-02-12 16:21:56				89	15.300	1.20	148
70238	2017-02-12 06:21:21				83	25.720	1.04	179
142970	2017-02-12 08:21:29				82	26.640	1.04	247
112833	2017-02-12 07:18:27				79	12.540	1.03	135
224970	2017-02-12 16:18:30				78	12.000	1.10	112
224971	2017-02-12 16:18:30				78	13.680	1.20	118

Fig. 7 Glass bead dispenser attached to a jig for stable and repeatable mounting on the ICEMET sensor

and D10 24.11 µm and D90 26.83 µm. Even though these results are well within the specifications given by the bead producer, further testing to evaluate the accuracy of the sensor is needed using a larger set of spheres with different sizes and repeated tests.
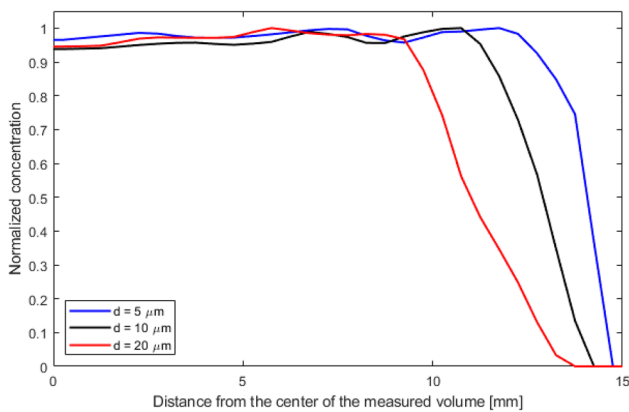
4.2 Sampling uniformity

The sampling uniformity of different sized droplets was simulated using a finite element method (FEM) in COMSOL software, with computational fluid dynamics (CFD) and particle tracing modules. The same experimental condition measurement results were obtained from a 3-min test run measurement from VTT Espoo icing wind tunnel, at the temperature of -5 °C. The measured LWC was 0.44 g/m^3 and MVD was 16 µm. The graphs are drawn as normalized concentration values, as no ground truth for the concentration is available at the wind tunnel. Both the simulations and the wind tunnel tests were made at 10 m/s wind speed,
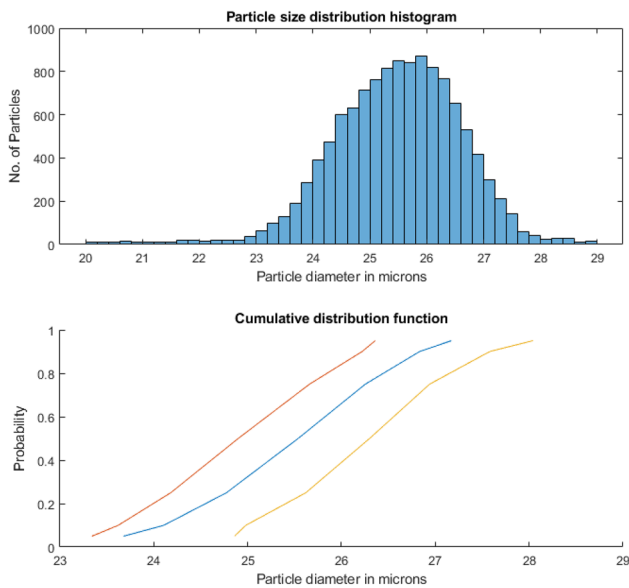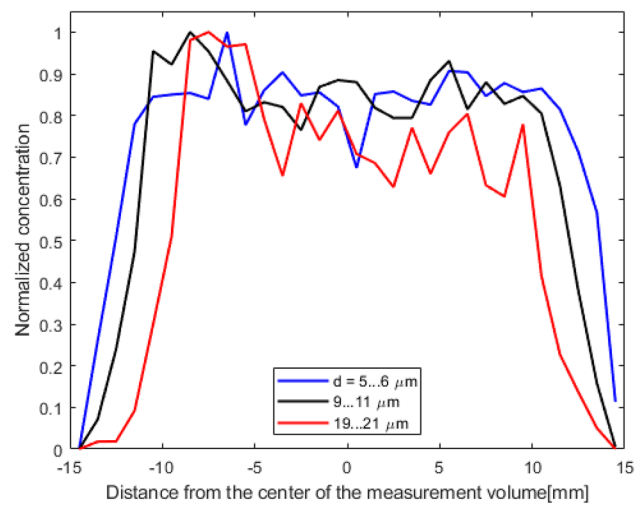
Fig. 8 ICEMET sensor sizing measurement verification results. The blue line is the measured particle size distribution by the ICEMET sensor, and the red and yellow line show the lower and upper NIST traceable lines for 95% confidence level (color figure online)
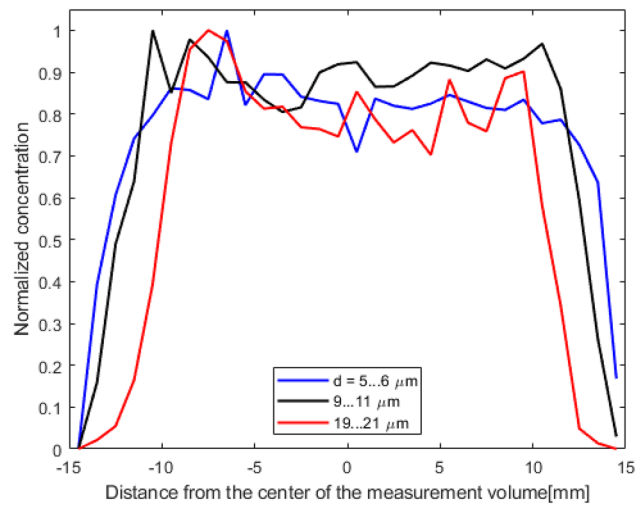

Fig. 10 The measured droplet concentrations at different distances measured from the center of the measurement volume along the optical axis from a 3-min run at wind speed of 10 m/s

Fig. 9 FEM simulations of three different sized droplets into a rectangular shaped measurement volume

Fig. 11 The measured droplet concentrations at different distances measured from the center of the measurement volume along the optical axis from a 24-min run at wind speed of 7 m/s

and from the measured data, size ranges near the simulated three particle diameters were selected to have larger amount of particles per each position bin. Both the simulation, Fig. 9 and the experimental result in Fig. 10, show similar variations near the walls inside the measurement volume.

The sampling of droplets is most uniform in these studies within the 20 mm wide center portion of the imaging volume. The sample area is different in simulations and in ICEMET measurement. The pyramid-shaped measurement volume is sampling different sized volumes at different locations along the optical axis. Thus, when measuring finite times of relatively sparse objects, such as cloud

droplets, it leads to a situation that larger droplet concentrations have larger variation (noise) on the laser side as fewer droplets are sampled. When comparing the 3-min test run at 10 m/s wind speed to the 24 min test run at 7 m/s wind speed in Fig. 11, it can be seen that the larger number of droplets clearly affects the concentration profile of 20 μm diameter range particles.

A benefit of using holographic technique in this case is that as the positions of all the found droplets are known, the sampling can be calibrated, and compensated as the 3D positions of the droplets are known. A benefit of using holographic imaging compared with conventional imaging is also that measurement volume can be defined numerically to be

Fig. 12 The image of the ICEMET sensor after the most harsh icing condition test run in the icing wind tunnel at VTT Espoo

just in the volume where the sampling is as close to isokinetic sampling as possible.

4.3 Anti-icing capability

The sensor anti-icing was tested in VTT icing wind tunnel at -5 °C and -15 °C temperatures, with wind speeds ranging from 4 to 20 m/s, and LWC ranging between 0.2 and 0.4 g/m^3 for test run lengths ranging from 3 to 25 min. In all tested conditions, the measurement volume surroundings were kept ice free, no ice build up on protective windows and the measurement was running without errors the whole time. In weak and moderate icing conditions, the whole sensor was ice free during the measurement, but in the most severe conditions tested, some ice was built mainly on the lower part of the frame where there is less heating power per surface area. A photo of the sensor immediately after 15-min run at -15 °C, LWC 0.185 g/m^3 and wind speed of 20 m/s shown in Fig. 12.

4.4 Field measurements

The ICEMET sensor was first tested in the field conditions when installed in Kivivaara-Peuravaara wind park on wind turbine nacelle in eastern Finland in November 2016, Fig. 13. The icing events were measured with an average sampling of 0.15 cm^3/s. The measurement were made starting in February and ending in the late April. The ICEMET sensor worked well during the whole period, no additional services were required for the ICEMET sensor during this period. The measured LWC and MVD values on ICEMET web user interface from an icing event taking place on 20th and 21st of March 2017 in Fig. 14.

Fig. 13 ▎ CEMET sensor installation on a wind turbine nacelle in 2017
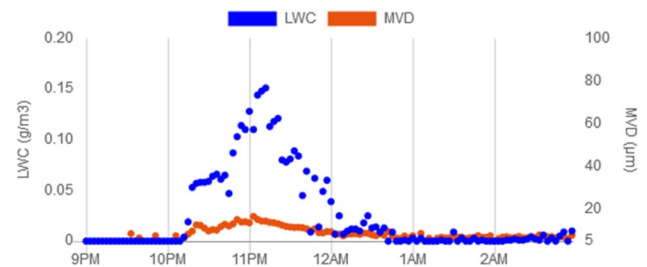
Fig. 14 The measured LWC and MVD values during an icing event on a wind turbine nacelle on 20th and 21th of March 2017
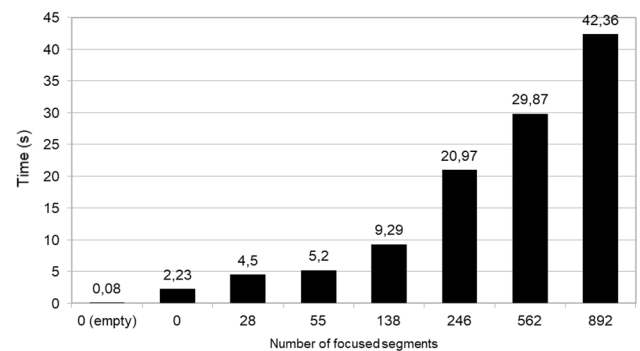
Fig. 15 ICEMET-server execution times per image with different droplet concentrations

4.5 Software performance

The performance measurements were made on a regular desktop computer with Intel Core i7-4770 CPU and NVIDIA GeForce RTX 2060 SUPER GPU. The results are presented in Fig. 15. It can be seen that the number of found segments where droplets are found directly affects the execution time. This is mainly caused by expensive

focus operations but also because of the limited writing speed of image files. A successful empty image detection in the preprocessing phase speeds up the process, because the reconstruction can be skipped. Typically in a single hologram, tens to a few hundreds of droplets are found, and the amount of droplets increases gradually over the time as an icing event starts. Thus, the ICEMET system can work as a very sensitive first warning system for icing conditions detection in real time with a suitable sampling rate in relation to the computational power.

5 Conclusions and discussion

The design of an optical holographic imager instrument for measuring cloud droplets and ice crystals was presented. The results from sizing verification, flow simulations, icing tunnel tests and field measurement tests showed that the proposed approach on measuring the LWC and DSD values during icing events in cold climate is possible and that the sensor design was proven to work in field conditions in real intended operating environment. Future work will be done to ensure the accuracy of the sizing and sampling of this type of instrument, using larger sizing standard sets and by comparing a wider range of computational fluid dynamics simulations of droplet trajectories in the measurement volume with the measured data with known wind speeds. The LWC and DSD data provided by the ICEMET sensor will be used to measure and model ice accretion on mechanical structures.

The presented approach to measure droplets would enable droplet positions at different times by multiple pulsed illumination [42]. This way the velocities of droplets for the icing rate calculation could be measured, if no separate wind speed measurement is present at the measurement site. In future, techniques such as the synthetic aperture (SA) imaging could be used in this type of low-cost measurement devices [43]. SA imaging could be used to enlarge the hologram recording area and thereby increasing the maximum resolving power and measurement volume using multiple image sensors, similarly it could be used to lower the component cost even further by replacing the 2/3″ sensor with multiple inexpensive image sensors.

References

1. Parent, O.: Ilinca A : anti-icing and de-icing techniques for wind turbines: critical review. Cold Reg. Sci. Technol. **65**(1), 88–96 (2011)
2. Makkonen, L.: Modeling of ice accretion on wires. J. Climate Appl. Meteorol. **23**(6), 929–939 (1984)
3. Krenn, A., Pieter, J.J., et al.: Available Technologies of Wind Energy in Cold Climates. Technical report, IEA Wind Task 19 (2016). https://community.ieawind.org/task19/viewdocument/iea-wind-tcp-task-19-available-tec?CommunityKey=b1ba65c9-bf79-4b55-98cd-cf324c26f76f&tab=librarydocuments
4. Fugal, J.P., Shaw, R.A., Saw, E.W., et al.: Airborne digital holographic system for cloud particle measurements. Appl. Opt. **43**(32), 5987–5995 (2004)
5. Baumgardner, D., Avallone, L., Bansemer, A., et al.: In situ, airborne instrumentation: addressing and solving measurement problems in ice clouds. Bull. Am. Meteorol. Soc. **93**(2), ES29–ES34 (2012)
6. Rydblom, S.: Thörnberg B : Liquid water content and droplet sizing shadowgraph measuring system for wind turbine icing detection. IEEE Sens. J. **16**(8), 2714–2725 (2016)
7. Sugimoto, N., Matsui, I., Shimizu, A.: Measurement of water cloud particle size with a dual-polarization pulsed bistatic lidar. Opt. Rev. **8**(6), 476–479 (2001)
8. Knollenberg, R.G.: The optical array: an alternative to scattering or extinction for airborne particle size determination. J. Appl. Meteorol. **9**(1), 86–103 (1970)
9. Henneberger, J., Fugal, J.P., Stetzer, O., et al.: HOLIMO II: a digital holographic instrument for ground-based in situ observations of microphysical properties of mixed-phase clouds. Atmos. Meas. Tech. **6**(11), 2975–2987 (2013)
10. Homola, M.C., Nicklasson, P.J., Sundsbø, P.A.: Ice sensors for wind turbines. Cold Reg. Sci. Technol. **46**(2), 125–131 (2006)
11. Jericho, S.K., Garcia-Sucerquia, J., Xu, W., et al.: Submersible digital in-line holographic microscope. Rev. Sci. Instrum. **77**(4), 043706 (2006). https://doi.org/10.1063/1.2193827
12. Watanabe, E., Hoshino, K., Takeuchi, S.: Portable digital holographic microscope using spherical reference beam. Opt. Rev. **22**(2), 342–348 (2015)
13. Tseng, D., Mudanyali, O., Oztoprak, C., et al.: Lensfree microscopy on a cellphone. Lab Chip **10**(14), 1787–1792 (2010)
14. Colomb, T., Cuche, E., Aspert, N., et al.: Wave front sensing method and apparatus US. Patent **7649**, 160 (2010)
15. Hinsch, K.D.: Holographic particle image velocimetry. Meas. Sci. Technol. **13**(7), R61 (2002)
16. Yu, X., Hong, J., Liu, C., et al.: Review of digital holographic microscopy for three-dimensional profiling and tracking. Opt. Eng. **53**(11), 112306 (2014)
17. Kubota, T.: 48 Years with holography. Opt. Rev. **21**(6), 883–892 (2014)

18. Gabor, D.: A new microscopic principle. Nature **161**(4098), 777 (1948)
19. Garcia-Sucerquia, J., Xu, W., Jericho, S.K., Jericho, M.H., Tamblyn, I., Kreuzer, H.J.: Digital in-line holography: 4-D imaging and tracking of micro-structures and organisms in microfluidics and biology. In: Proceedings of SPIE, ICO20: Biomedical Optics, vol. 6026 (2006). https://doi.org/10.1117/12.667447
20. Uhlig, E., Borrmann, S., Jaenicke, R.: Holographic in-situ measurements of the spatial droplet distribution in stratiform clouds. Tellus B **50**(4), 377–387 (1998)
21. Chambers, T.E., Hamilton, M.W., Reid, I.M.: A low-cost digital holographic imager for calibration and validation of cloud microphysics remote sensing. In: Anonymous Remote Sensing of Clouds and the Atmosphere XXI, 10001 vol. International Society for Optics and Photonics (2016)
22. Thompson, B.J., Ward, J.H., Zinky, W.R.: Application of hologram techniques for particle size analysis. Appl. Opt. **6**(3), 519–526 (1967)
23. Garcia-Sucerquia, J., Xu, W., Jericho, S.K., et al.: Digital in-line holographic microscopy. Appl. Opt. AO. **45**(5), 836–850 (2006). https://doi.org/10.1364/AO.45.000836
24. Schnars, U., Jüptner, W.: Digital holography. Springer, Berlin (2005)
25. American meteorological society: Glossary of meteorology: droplet. https://glossary.ametsoc.org/wiki/Droplet. Accessed 27 Sep 2019
26. Best, A.: Drop-size distribution in cloud and fog. Q J R Meteorol. Soc. **77**(333), 418–426 (1951)
27. Finstad, K.J., Lozowski, E.P., Makkonen, L.: On the median volume diameter approximation for droplet collision efficiency. J. Atmos. Sci. **45**(24), 4008–4012 (1988)
28. Kollár, L.E., Farzaneh, M., Karev, A.R.: Modeling droplet collision and coalescence in an icing wind tunnel and the influence of these processes on droplet size distribution. Int. J. Multiph. Flow **31**(1), 69–92 (2005)
29. Makkonen, L.: Models for the growth of rime, glaze, icicles and wet snow on structures. Philosophical transactions of the Royal Society of London. Series A **358**(1776), 2913–2939 (2000)
30. Noone, K.J., Charlson, R.J., Covert, D.S., et al.: Cloud droplets: solute concentration is size dependent. J. Geophys. Res. **93**(D8), 9477–9482 (1988)
31. Spuler, S.M., Fugal, J.: Design of an in-line, digital holographic imaging system for airborne measurement of clouds. Appl. Opt. **50**(10), 1405 (2011). https://doi.org/10.1364/AO.50.001405
32. Meier, O., Scholz, D.: A Handbook Method for the Estimation of Power Requirements for Electrical De-Icing Systems. Deutscher Luft und Raumfahrtkongress (DLRK), 31st August–2nd September 2010, Hamburg, Germany. DocumentID 161191 (2010). https://www.fzt.haw-hamburg.de/pers/Scholz/MOZART/MOZART_PUB_DLRK_10-08-31.pdf, http://mozart.profscholz.de/
33. Molkoselkä, E.O.: Icemet-server: Hologram processing and cloud droplet analysis software for ICEMET-project. https://github.com/molkoback/icemet-server (2019). Accessed 19 Sep 2019
34. Khronos Group: The open standard for parallel programming of heterogeneous systems. https://www.khronos.org/opencl/. Accessed 19 Dec 2019
35. Fugal, J.P., Schulz, T.J., Shaw, R.A.: Practical methods for automated reconstruction and characterization of particles in digital in-line holograms. Meas. Sci. and Technol. **20**(7), 075501 (2009)
36. Pan, G., Meng, H.: Digital holography of particle fields: reconstruction by use of complex amplitude. Appl. Opt. **42**(5), 827–833 (2003)
37. Kim, M.K.: Principles and techniques of digital holographic microscopy. SPIE Rev. **1**(1), 018005 (2010)
38. Meng, H., Anderson, W.L., Hussain, F., et al.: Intrinsic speckle noise in in-line particle holography. JOSA A **10**(9), 2046–2058 (1993)
39. Cheong, F.C., Krishnatreya, B.J., Grier, D.G.: Strategies for three-dimensional particle tracking with holographic video microscopy. Opt. Express **18**(13), 13563–13573 (2010)
40. Öhman, J., Sjödahl, M.: Off-axis digital holographic particle positioning based on polarization-sensitive wavefront curvature estimation. Appl. Opt. **55**(27), 7503–7510 (2016)
41. Droplet Measurement Technologies Inc: PADS operator manual. https://www.dropletmeasurement.com/PADS_Help/MVD_(um).htm (2010). Accessed 29 Sep 2019
42. Satake, S., Kunugi, T., Sato, K., et al.: Three-dimensional flow tracking in a micro channel with high time resolution using micro digital-holographic particle-tracking velocimetry. Opt. Rev. **12**(6), 442–444 (2005)
43. Ishi, Y., Komatsu, S.: Synthetic aperture digital holography with cross-correlation of reconstruction images. Opt. Rev. **19**(4), 228–234 (2012)